THERMAL PHOTONICS

Localized thermal emission from topological interfaces

M. Said Ergoktas[1,2], Ali Kecebas[3], Konstantinos Despotelis[1,2]†, Sina Soleymani[3], Gokhan Bakan[1,2], Askin Kocabas[4], Alessandro Principi[5], Stefan Rotter[6], Sahin K. Ozdemir[3,7], Coskun Kocabas[1,2,8]*

The control of thermal radiation by shaping its spatial and spectral emission characteristics plays a key role in many areas of science and engineering. Conventional approaches to tailoring thermal emission using metamaterials are hampered both by the limited spatial resolution of the required subwavelength material structures and by the materials' strong absorption in the infrared. In this work, we demonstrate an approach based on the concept of topology. By changing a single parameter of a multilayer coating, we were able to control the reflection topology of a surface, with the critical point of zero reflection being topologically protected. The boundaries between subcritical and supercritical spatial domains host topological interface states with near-unity thermal emissivity. These topological concepts enable unconventional manipulation of thermal light for applications in thermal management and thermal camouflage.

A concept that has recently emerged in the field of non-Hermitian photonics (*1*–*3*) is that of coherent perfect absorption (*4*–*8*), which has been conceptualized as the time-reversed process of a laser operating at its first lasing threshold (*4*, *9*). In the same way as a laser cavity emits coherent light with a sufficient amount of gain, the same cavity will turn into a coherent perfect absorber (CPA) with the same amount of negative gain (i.e., loss). In this work, we extended this concept for thermal emitters, for which Kirchhoff's law of thermal radiation directly links the thermally induced emissivity (ε, gain) of a material with its absorptivity (α, loss) at thermal equilibrium (*10*–*12*). For broadband and incoherent radiation, this reciprocity relation has the well-known consequence that a perfect thermal emitter is a blackbody that perfectly absorbs light at all frequencies (*13*). In turn, designing a perfect thermal emitter for coherent radiation at a single frequency involves the creation of a CPA for light incident right at the desired frequency value. Moreover, for single-sided illumination, such a CPA can be realized by an optical cavity at the critical coupling condition (*8*, *14*). To guarantee the coherence of the perfect emission (ε = 1) of this critically coupled cavity, the coherence length of the thermal radiation must be longer than the length associated with a cavity round trip (*10*).

[1]Department of Materials, University of Manchester, Manchester M13 9PL, UK. [2]National Graphene Institute, University of Manchester, Manchester M13 9PL, UK. [3]Department of Engineering Science and Mechanics, The Pennsylvania State University, University Park, PA 16802, USA. [4]Department of Physics, Koç University, Istanbul, Türkiye. [5]Department of Physics, University of Manchester, Manchester M13 9PL, UK. [6]Institute for Theoretical Physics, Vienna University of Technology (TU Wien), 1040 Vienna, Austria. [7]Materials Research Institute, The Pennsylvania State University, University Park, PA 16802, USA. [8]Henry Royce Institute for Advanced Materials, University of Manchester, Manchester M13 9PL, UK.
*Corresponding author. Email: coskun.kocabas@manchester.ac.uk
†Present address: National Physical Laboratory, Teddington TW11 0LW, UK.

Cavity design

To implement the concept of a topologically protected perfect thermal emitter at a well-defined frequency, we used a lossy optical cavity (Fig. 1A). A thin (thickness t < 20 nm) platinum (Pt) layer acts both as a broad-band thermal emitter with controllable thermal emissivity and as a cavity mirror with tunable reflectivity. We emphasize that the emissivity ε of a free-standing thin film is fundamentally restricted to values less than 0.5 (*15*). However, placing the thin film near a strongly reflecting (metallic) substrate enables coherent interference of the thermal radiation emanating from the top and bottom sides of the film's surface, resulting in emissivity values greater than 0.5 at certain wavelengths. For the realization of the strongly reflecting substrate (back mirror), we used a thick layer of gold behind a 2-μm dielectric spacing layer of parylene-C that is transparent in the infrared (IR). The emissivity of the back mirror (<0.05) and that of the dielectric layer have negligible effects on the overall emissivity of the cavity.

Topological tuning of thermal emission

Precise tuning of the thickness of the Pt film reveals unity emissivity at the critical thickness $t_c \approx 2.3$ nm, as detailed in Fig. 1, B and C. This condition of perfect emission is not just a coincidental phenomenon; rather, it is of topological origin (*16*–*18*). The topological aspects of the phase transition that occur when crossing the point of critical coupling becomes evident in the complex representation of the frequency-dependent Fresnel reflection coefficient $r(\omega)$, as depicted in Fig. 1D. Here, the reflection spectrum exhibits periodic resonances, represented as recurring circles in the complex plane. With extremely thin films (t < 1 [illegible] subcritical coupling), the reflection spectrum forms a small circle near $r = -1$, corresponding to the reflective properties of a perfect electric conductor. At the critical thickness, $t_c \approx 2.3$ nm, the reflection spectrum intersects the origin, resulting in zero reflection and, correspondingly, unity emissivity and unity absorption. For thicknesses exceeding t_c (supercritical coupling), the reflection spectrum encircles the origin, which is indicative of a transition to a nontrivial topological phase. As the thickness of the Pt is tuned, the surface's reflection transitions from resembling an electrical conductor to mimicking a magnetic conductor with nontrivial reflection topology. In this context, the topological invariant is the winding number (*19*), defined as $w = \frac{1}{2\pi}\oint d\varphi$, where the phase $\varphi = \arg[r(\omega)]$ of the Fresnel reflection coefficient is integrated here over the cavity's free spectral range (1325 cm^{-1}). Although this phase is not defined at the origin, $r(\omega) = 0$, the fact that this critical point is encircled for supercritical cavities, but not for subcritical ones, divides the system into two different topological classes.

To investigate the characteristics of thermal emission, we utilized a Fourier transform infrared spectrometer (FTIR) using the sample itself as a heat source and measured the first-order temporal correlations of the emitted IR light. We observed an enhancement in the visibility of the interferograms precisely at the transition point (i.e., critical coupling point), a compelling indicator of an extended coherence length of the emission (*15*).

Further insight is provided in the inset of Fig. 1D, which illustrates the phase singularity in the parameter space that occurs when the radiative loss, Γ_r, precisely matches the cavity's intrinsic loss, Γ_i. The reflection coefficient of the cavity is calculated using the coupled mode theory (*16*) as $r = -1 + \frac{2\Gamma_r}{-i(\omega-\omega_0)+\Gamma_i+\Gamma_r}$, where ω_0 is the resonance frequency defined by the length of the cavity. The thickness of the thermal emitting layer defines both intrinsic ($\Gamma_i \propto t$) and radiative loss $\left(\Gamma_r \propto \frac{1}{t}\right)$ of the cavity. Fine-tuning of the metal thickness thus enables a continuous transition from trivial to nontrivial topology in the reflection coefficient. Because the phase singularity is a point in parameter space, the unity emissivity appears at the resonance frequency. The angular and spectral response of the cavity could be extended by using a degenerate cavity (*20*) or by coupling to an exceptional point degeneracy in the cavity (*21*).

To analyze the reflection phase, we built a phase-sensitive FTIR to enable the direct placement of the sample within the interferometer (as depicted in Fig. 2A) and measured the reflection phase for various thicknesses of Pt. This setup facilitates the acquisition of an interferogram, which effectively captures the first-order correlation between the reference

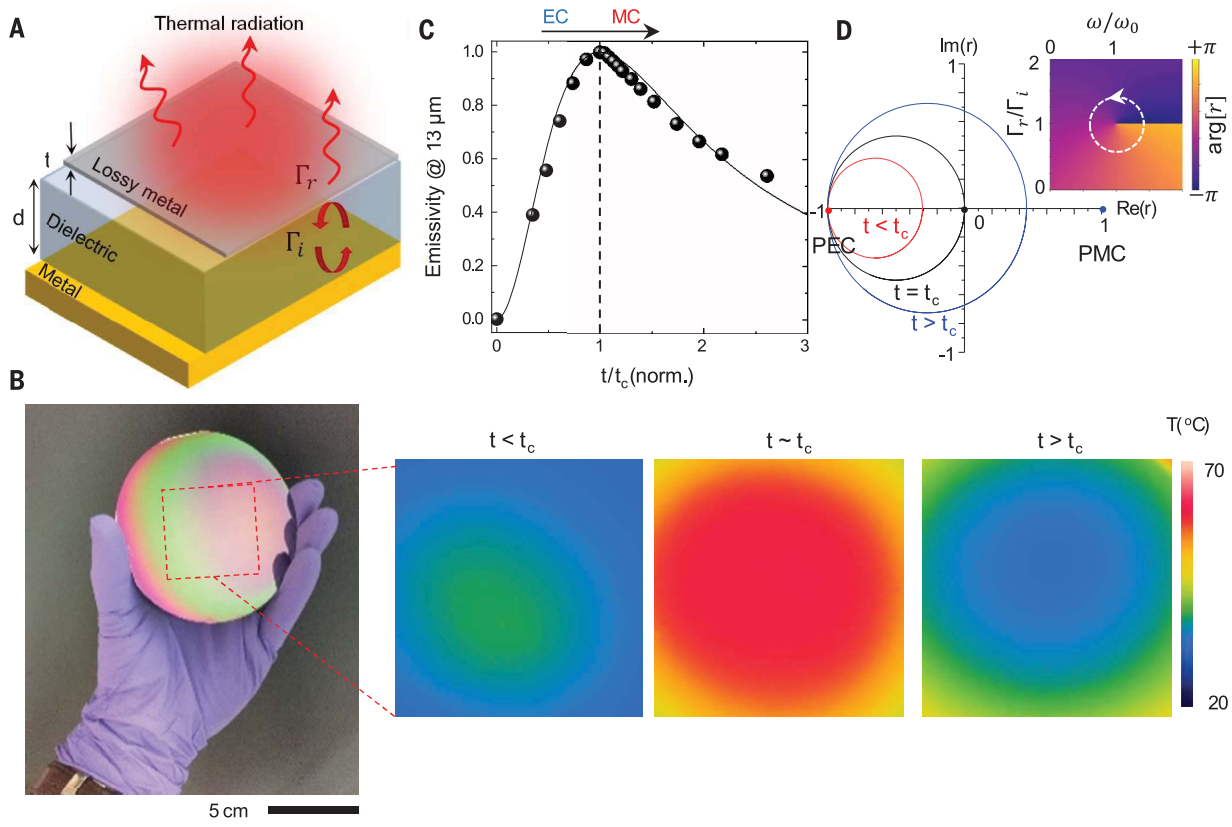

Fig. 1. Topological phase transition in a thermal emitter. (**A**) Schematic of the thermal emitting surface, which consists of a lossy metal (top surface, thickness t) separated by a dielectric layer (d) from a metallic substrate (bottom surface). The thermal radiation from this lossy cavity shows topologically distinct behavior defined by the balance between radiative Γ_r and intrinsic Γ_i losses as controlled by the thickness t of the top metal film. (**B**) Photograph of the sample (left) and its IR camera images showing the variation of thermal radiation from the surface for three different thickness (right). IR images were recorded from a sample placed on a hot plate at 70°C. At a critical thickness ($t_c \approx 2.3$ nm), we observed near-perfect thermal emissivity ($\varepsilon \approx 1$). (**C**) Variation of the far-IR thermal emissivity ($\lambda = 13$ μm) as a function the thickness t of the lossy metal on top. The solid line shows the emissivity calculated by the model. EC, electrical conductor; MC, magnetic conductor. (**D**) The complex reflectivity spectra $r(\omega)$ for the three cases of subcritical (red), critical (black), and supercritical (blue) coupling. The inset shows the reflection phase in parameter space around the critical coupling point, $r_c = 0$, where a phase vortex appears, and intrinsic cavity losses are matched by the radiative losses. PEC, perfect electric conductor; PMC, perfect magnetic conductor.

beam and the beam reflected by the sample, thereby yielding a direct measurement of the complex Fresnel reflection coefficient. Figure 2, B and C, represents the magnitude $|r(\omega)|$ and the phase $\varphi = \arg[r(\omega)]$ of the reflection coefficient for the IR spectrum covering the first five cavity modes. Notably, the topological difference is manifested in the phase spectra; the reflection phase from the trivial surface reverts to its original state, whereas the nontrivial surface exhibits a cumulative phase increment of 2π for each resonance. This 2π-phase is a non-Hermitian generalization of the Berry phase (*22*) that originates from the winding number. The critical thickness shows slight variation for different modes due to the wavelength dependence of intrinsic loss of the cavity. Further, in Fig. 2D, we present the complex reflection spectrum for the third mode, comparing the results for the two distinct topologies. Figure 2E shows the singularity of the zero reflection in the parameter space. The phase map, displaying φ versus ω with periodic boundary conditions for both axes, is homeomorphic to the surface of a torus with genus one, as depicted in Fig. 2F. When the phase spectrum of reflection is represented on a toroidal surface, it offers a distinct method to visualize topological differences. The red and blue curves represent the phase spectra of trivial and nontrivial surfaces, respectively. These curves, which are not isotopic on the torus surface, illustrate the differing topologies. They cannot be continuously mapped onto each other (*15*).

On the most fundamental level, the topological origin of perfect emissivity at critical coupling reveals itself when considering the interface between topologically distinct regions (*23*–*26*), such as between a subcritically and a supercritically coupled cavity. This is because the transition of a topological invariant such as the winding number across such a boundary requires the presence of a phase singularity with $r(\omega) = 0$ at the interface. Owing to reciprocity, this line of phase singularity in the absorption is accompanied by a topologically protected interface state with perfect thermal emissivity. We implemented such a localized edge state of high-intensity thermal emission on a low-emissivity surface by controlling the film thickness t in a stepwise way such that topologically inequivalent areas are formed, whose boundaries will be shown to confine the thermal emission. Furthermore, this line of phase singularity would support chiral waveguide states that can be excited by an external light source (*27*).

Thermal emission at a boundary

To visually capture these boundaries, we fabricated an optical surface on a silicon wafer characterized by two distinct reflection topologies that establish a visible boundary at the wafer's center (Fig. 3A). To render the interface emission with a far-IR camera, we calibrated the dielectric layer's thickness, aligning the resonance wavelength (~10 μm) with the camera's

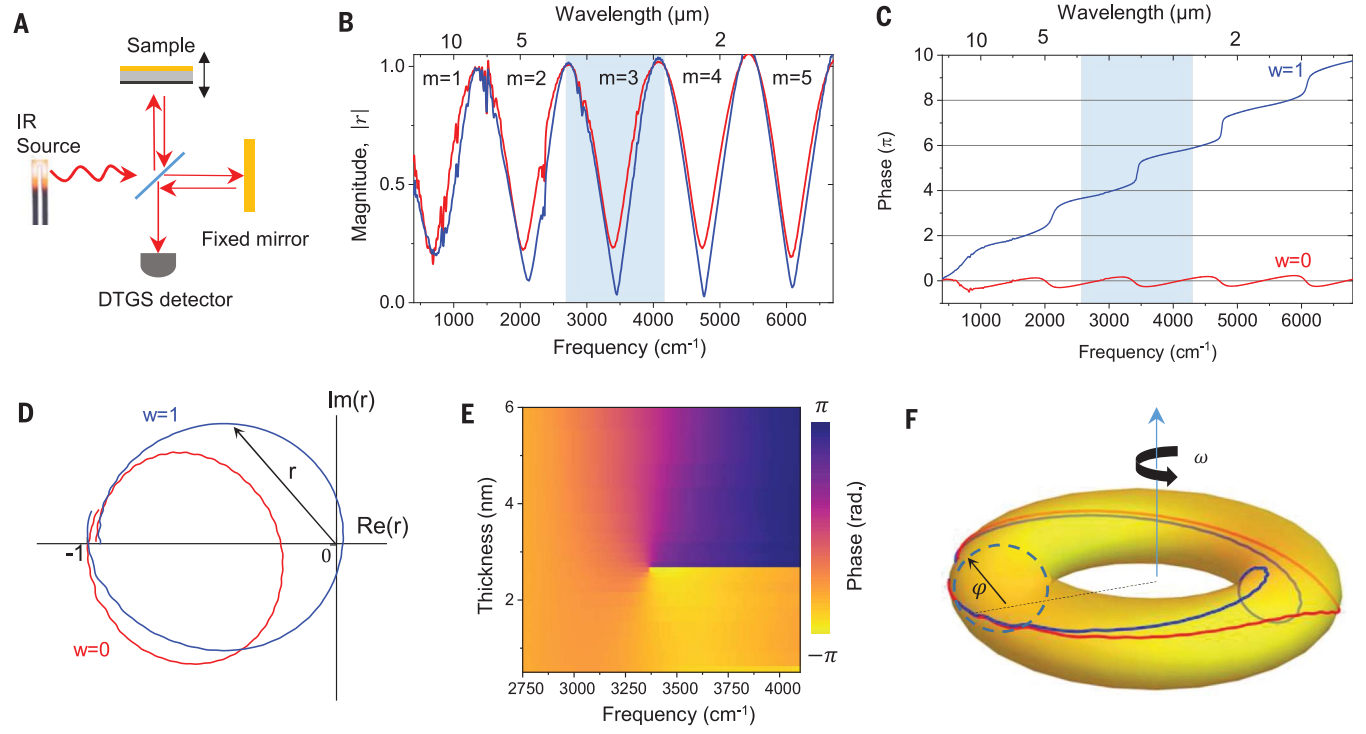

Fig. 2. Spectroscopic assessment of topological phase transition. (**A**) Experimental configuration using a phase-sensitive FTIR, with the sample functioning as a dynamic mirror within the Michelson interferometer. DTGS, deuterated triglycine sulfate. (**B** and **C**) Magnitude $|r(\omega)|$ (B) and phase $\varphi(\omega)$ (C) spectra of the Fresnel reflection coefficient for trivial (red curve; winding number $w = 0$, $t = 2.0$ nm) and nontrivial (blue curve; $w = 1$, $t = 2.7$ nm) surfaces, revealing periodic resonance modes (m) that possessing a free spectral range of 1325 cm^{-1}. (**D**) A complex representation of the measured reflection coefficient $r(\omega)$ depicts two distinct winding numbers, 0 and 1, for thicknesses when $t < t_c$ and $t > t_c$, respectively. (**E**) Experimentally obtained map of the reflection phase, highlighting a singularity endowed with a topological charge of +1. (**F**) Spectrum of the reflection phase mapped on to the surface of a torus. Here, φ is the reflection phase, and the rotation over the toroidal angle ϕ represents frequency over a free spectral range of the cavity. The red and blue curves are not isotopic on the surface of the torus, indicating different topologies.

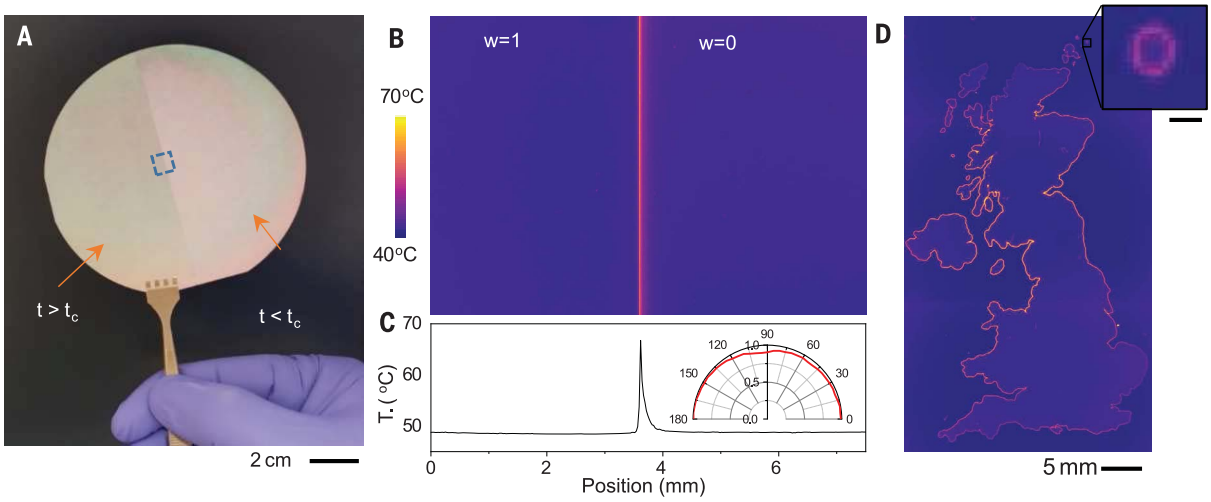

Fig. 3. Localized thermal emission from a topological interface. (**A**) Photograph of the sample, which includes a boundary between topologically distinct domains. (**B**) IR thermogram obtained from the blue dashed square region shown in (A), illustrating intense thermal emission localized at the boundary. (**C**) Profile of the recorded temperature (T) across the boundary, revealing localized emission. Although both domains exhibit low thermal emissivity, the boundary itself presents an emissivity value of 1. The inset details the negligible polarization dependence of the emissivity. (**D**) IR thermogram displaying thermal radiation along the boundary of a complex shape (map of the United Kingdom). Here, the different domains on either side of the boundary are realized by trivial and nontrivial topological phases, respectively, with the thermal radiation continuously tracing the map's contour. The inset provides a magnified view of an island surrounded by a continuous boundary mode. The scale bar in the inset is 100 μm.

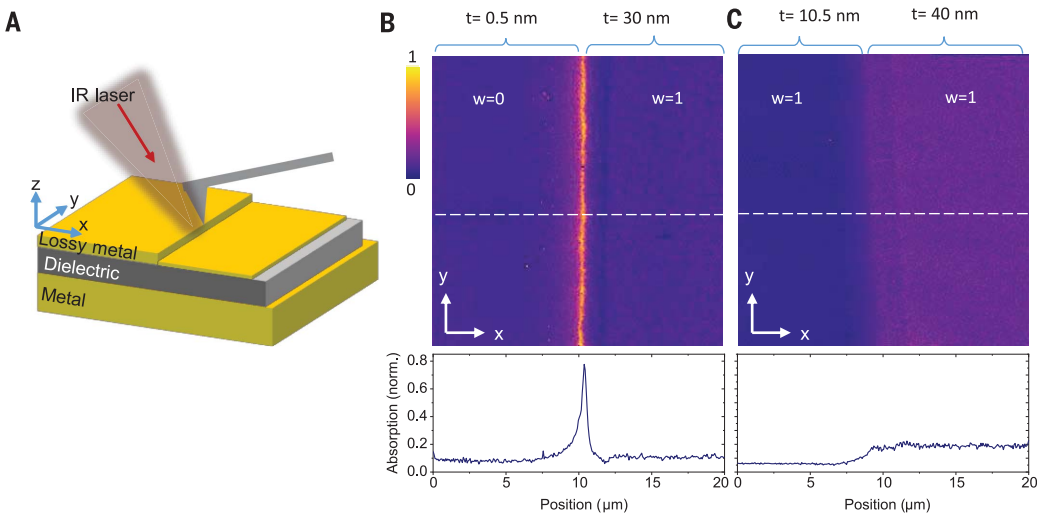

Fig. 4. NanoIR spectroscopy of the topological edge mode. (**A**) Schematic drawing of the sample geometry and the AFM-IR setup we used to measure the local force generated by the photothermal expansion. (**B** and **C**) Resonance-enhanced contact mode AFM-IR images and IR absorption profiles of a boundary between topologically different (B) and identical (C) domains. The images were obtained at the excitation wave number of 850 cm^{-1}. The white dashed lines indicate the cross section along which the absorption profiles shown in the lower panels are obtained.

spectral window (8 to 14 μm). Despite both metal thicknesses yielding low thermal emissivity (0.2 and 0.3), a pronounced, unpolarized thermal emission was observed at their interface (Fig. 3B). It is important to mention that at the resonance frequency, one side of the boundary functions as an electrical conductor $\{\varphi = \arg[r(\omega_0)] = \pi\}$, whereas the opposite side operates as a magnetic conductor $\{\varphi = \arg[r(\omega_0)] = 0\}$, both of which exhibit low thermal emissivity. However, the interface itself serves as a dipole owing to the out-of-phase response on both sides when the topologies differ. This thermal emissivity at the boundary emerges exclusively when there is a change in the winding number across the boundary (*16*). Additionally, we note that the thermal radiation emitted from these modes is unpolarized (inset in Fig. 3C). Given that these lines of perfect emission $[\varepsilon(\omega_0) = 1]$ at the boundary are protected by the reflection topology, they exhibit robustness against local perturbations and defects. This resilience is shown by a more intricate shape—the map of the United Kingdom (defined by photolithography and metallization)—realized by different metal thicknesses inside and outside of the country's borders. A continuous line of thermal emission that traces the map's boundary is clearly observable, as can be seen from the enlarged image in Fig. 3D, which shows a small island surrounded by a line of thermal emission at its boundary. The interface state follows the complicated boundary down to the spatial resolution of the IR camera (~25 μm) and the fidelity of the photolithography process.

Probing localized thermal emission

To precisely probe the spatial distributions of localized emission, we used nanoscale infrared (nanoIR) photothermal spectroscopy (*28*, *29*), facilitated by an atomic force microscope (AFM) integrated with a broadband tunable IR laser (Fig. 4A). This technique yields direct measurements of nanoscale IR absorption (*15*). The AFM cantilever registers the photothermal expansion, an indicator that is directly proportional to IR absorption, thereby offering insights into local IR emissivity. We first recorded the resonance-enhanced contact-mode AFM-IR image (Fig. 4B) at the boundary that separates regions with top metal layers with thicknesses of 0.5 and 30 nm. We observed that the localized absorption at the boundary exhibits an exceptionally narrow spatial distribution (approximately 1 μm, or ~λ/10). This distinctive mode was present for both transverse electric and transverse magnetic polarized laser excitations. After these observations, we deposited an additional 10 nm of metal onto the sample, effectively increasing the top metal thickness in these regions to 10.5 and 40 nm, respectively, surpassing the critical thickness (t_c = 2.8 nm) and rendering their reflection topologies identical. Under these modified conditions, the previously detected edge mode disappeared (Fig. 4C), demonstrating that these protected modes manifest themselves exclusively at topological boundaries where the winding number makes a step change.

The hallmark of topological boundaries is their ability to support chiral edge modes. However, with our experimental setup, we cannot excite and visualize these modes. To investigate this feature, we performed three-dimensional finite-difference simulations by placing a chiral dipole emitter positioned in the near field of the boundary. Our simulations show that the topological boundary between domains with different winding numbers supports counterpropagating chiral edge modes (*15*). These localized modes show strong spin-momentum locking (*26*), resembling the edge modes found in photonic metasurfaces with band inversion (*31*–*34*) and on-Hermitian line modes (*25*). It is important to note that these interfaces support two counterpropagating edge modes that could be backscattered with a certain type of defect (*15*, *34*). For a non-Hermitian system, the interface with a topological number contrast of 1 would support two edge modes (*35*). Future work should aim to observe these chiral edge modes not only at IR but also at wavelength ranges extended to near-IR or even visible. Furthermore, the presence of these modes is contingent on the balance between inherent and radiative losses in the cavity. Adjusting the spatial variation of material's loss through an external field could lead to the adaptable paths for these edge modes, thus facilitating the directed transmission of IR signals. This property could be achieved by materials with tunable IR absorption enabling reconfigurable routing.

Conclusions

Our framework for the design of thermal emitters shows that a state of perfect absorption emerges from a topological phase transition characterized by a change in the winding number, that is, a topological invariant. Despite the origin of thermal radiation being spontaneous emission from uncorrelated sources, the emergence of topological features offers new design strategies for thermal photonics (*36*). Unlike conventional topological photonic systems that rely on topology of the band structure of photonic crystals, our approach does not require any periodic structure to explore topological features. Stepping away from the constraints of periodicity would enable broader applications of topological phenomena.

REFERENCES AND NOTES

1. C. E. Rüter *et al.*, *Nat. Phys.* **6**, 192–195 (2010).
2. M. A. Miri, A. Alù, *Science* **363**, eaar7709 (2019).
3. Ş. K. Özdemir, S. Rotter, F. Nori, L. Yang, *Nat. Mater.* **18**, 783–798 (2019).
4. Y. D. Chong, L. Ge, H. Cao, A. D. Stone, *Phys. Rev. Lett.* **105**, 053901 (2010).
5. W. Wan *et al.*, *Science* **331**, 889–892 (2011).
6. D. G. Baranov, A. Krasnok, T. Shegai, A. Alù, Y. Chong, *Nat. Rev. Mater.* **2**, 17064 (2017).
7. C. Wang, W. R. Sweeney, A. D. Stone, L. Yang, *Science* **373**, 1261–1265 (2021).
8. S. Soleymani *et al.*, *Nat. Commun.* **13**, 599 (2022).
9. K. Pichler *et al.*, *Nature* **567**, 351–355 (2019).

10. J. J. Greffet *et al*., *Nature* **416**, 61–64 (2002).
11. W. Li, S. Fan, *Opt. Express* **26**, 15995–16021 (2018).
12. P. N. Dyachenko *et al*., *Nat. Commun.* **7**, 11809 (2016).
13. K. Mizuno *et al*., *Proc. Natl. Acad. Sci. U.S.A.* **106**, 6044–6047 (2009).
14. N. Kumar Gupta *et al*., *J. Opt.* **17**, 035003 (2015).
15. See supplementary materials.
16. M. Liu *et al*., *Phys. Rev. B* **107**, L241403 (2023).
17. G. Ermolaev *et al*., *Nat. Commun.* **13**, 2049 (2022).
18. C. Guo, J. Li, M. Xiao, S. Fan, *Phys. Rev. B* **108**, 155418 (2023).
19. M. S. Ergoktas *et al*., *Science* **376**, 184–188 (2022).
20. Y. Slobodkin *et al*., *Science* **377**, 995–998 (2022).
21. S. Soleymani *et al*., *Nat. Commun.* **13**, 599 (2022).
22. W. P. Su, J. R. Schrieffer, A. J. Heeger, *Phys. Rev. Lett.* **42**, 1698–1701 (1979).
23. S. Barik *et al*., *Science* **359**, 666–668 (2018).
24. M. Moccia, G. Castaldi, A. Alù, V. Galdi, *ACS Photonics* **7**, 2064–2072 (2020).
25. K. Y. Bliokh, D. Smirnova, F. Nori, *Science* **348**, 1448–1451 (2015).
26. M. Asano *et al*., *Nat. Commun.* **7**, 13488 (2016).
27. K. Y. Bliokh, D. Leykam, M. Lein, F. Nori, *Nat. Commun.* **10**, 580 (2019).
28. A. Dazzi, C. B. Prater, *Chem. Rev.* **117**, 5146–5173 (2017).
29. A. Centrone, *Annu. Rev. Anal. Chem.* **8**, 101–126 (2015).
30. H. Zhao *et al*., *Science* **365**, 1163–1166 (2019).
31. L. H. Wu, X. Hu, *Phys. Rev. Lett.* **114**, 223901 (2015).
32. D. Smirnova *et al*., *Phys. Rev. Lett.* **123**, 103901 (2019).
33. S. Guddala *et al*., *Science* **374**, 225–227 (2021).
34. C. A. Rosiek *et al*., *Nat. Photonics* **17**, 386–392 (2023).
35. D. Leykam, K. Y. Bliokh, C. Huang, Y. D. Chong, F. Nori, *Phys. Rev. Lett.* **118**, 040401 (2017).
36. M. S. Ergoktas *et al*., *Nat. Photonics* **15**, 493–498 (2021).
37. M. S. Ergoktas *et al*., Localized thermal emission from topological interfaces. Zenodo (2024); https://doi.org/10.5281/zenodo.10829942.

ACKNOWLEDGMENTS

We thank the Henry Royce Institute for Advanced Materials for the use of their scanning probe microscopy facility. **Funding:** This work was funded through the European Research Council through ERC-Consolidator grant 682723 and EPSRC EP/X027643/1 (ERC PoC grant) and an Air Force Office of Scientific Research (AFOSR) Multidisciplinary University Research Initiative (MURI) Award on Programmable Systems with non-Hermitian Quantum Dynamics (award FA9550-21-1-0202). S.K.O. and A.Ko. acknowledge support from AFOSR awards FA9550-18-1-0235 and FA9550-22-1-0431. A.P. acknowledges support from the European Commission under the EU Horizon 2020 MSCA-RISE-2019 program (project 873028 HYDROTRONICS) and from the Leverhulme Trust under grant agreements RPG-2019-363 and RPG-2023-253. **Author contributions:** M.S.E. and C.K. conceived the idea. M.S.E. fabricated the samples. M.S.E. and C.K. carried out the experiments. K.D. performed nanoIR measurements. A.Ke. and S.S. performed the electromagnetic simulations. G.B., A.P., and A.Ko. provided theoretical support. M.S.E., S.R., S.K.O., and C.K. analyzed the data and wrote the manuscript with input from all authors. C.K. and S.K.O. supervised the project. **Competing interests:** The authors declare no competing financial interests. **Data and materials availability:** All data discussed in the main text and the code used in the simulations are available at Zenodo (*37*).

SUPPLEMENTARY MATERIALS

science.org/doi/10.1126/science.ado0534
Materials and Methods
Figs. S1 to S11
Movies S1 to S3

Submitted 16 January 2024; accepted 19 April 2024
10.1126/science.ado0534